

## Journal Pre-proofs

CFD Simulation for Characterization and Scale-Up of Pulsed Biomass Transport

Lucas Massaro Sousa, Benjamin Amblard, Sina Tebianian

PII: S0009-2509(22)00236-6  
DOI: <https://doi.org/10.1016/j.ces.2022.117652>  
Reference: CES 117652

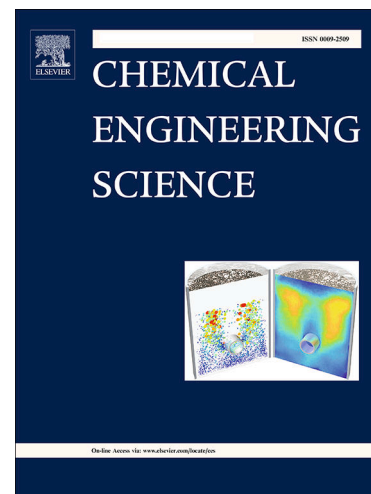
To appear in: *Chemical Engineering Science*

Received Date: 15 December 2021  
Revised Date: 28 March 2022  
Accepted Date: 1 April 2022

Please cite this article as: L. Massaro Sousa, B. Amblard, S. Tebianian, CFD Simulation for Characterization and Scale-Up of Pulsed Biomass Transport, *Chemical Engineering Science* (2022), doi: <https://doi.org/10.1016/j.ces.2022.117652>

This is a PDF file of an article that has undergone enhancements after acceptance, such as the addition of a cover page and metadata, and formatting for readability, but it is not yet the definitive version of record. This version will undergo additional copyediting, typesetting and review before it is published in its final form, but we are providing this version to give early visibility of the article. Please note that, during the production process, errors may be discovered which could affect the content, and all legal disclaimers that apply to the journal pertain.

© 2022 Elsevier Ltd. All rights reserved.



A revised manuscript for publication in  
Chemical Engineering Science

# CFD Simulation for Characterization and Scale-Up of Pulsed Biomass Transport

Lucas Massaro Sousa<sup>1,2</sup>, Benjamin Amblard<sup>1</sup>, Sina Tebianian<sup>1\*</sup>

<sup>1</sup>Process Design and Modeling Division, IFP Energies Nouvelles, Rond-Point Échangeur de Solaize, 69360 Solaize, France

<sup>2</sup>Wolfson Centre for Bulk Solids Handling Technology, Faculty of Engineering & Science, University of Greenwich, Central Avenue, Chatham ME4 4TB, UK

---

\* Corresponding author. E-mail addresses : sina.tebianian@ifpen.fr (S. Tebianian),  
L.MassaroSousa@gre.ac.uk (L. Massaro Sousa)

**ABSTRACT**

Stable feeding of biomass powders into reactors represents a technical operational challenge for renewable energy generation. The injection of sawdust powders has been recently published with a horizontal pressurized gas injector under several experimental conditions. Valid numerical models are useful for hydrodynamic characterization of different equipment scales, such as computational fluid dynamics (CFD). In this study, the applicability of the CFD multiphase particle-in-cell approach (MP-PIC) for the considered injector is investigated. The model is tested under different operating conditions, showing relative deviations lower than 14% and 2% for solids flux and flow concentration experimental data. The effect of model inputs (mesh refinement, drag model, particle-to-wall interaction) on the system's hydrodynamics is discussed. The gas-solid flow hydrodynamics is obtained from the simulations providing additional insight on pulsed biomass transport. Ultimately, the model is used to investigate different injector diameters and to propose a feeder operation map as a function of dimensionless parameters.

**Keywords:** CFD, MP-PIC, Barracuda, pneumatic transport, bulk solids handling, non-mechanical feeder.

## 1 Introduction

Solid biomass wastes are generated in large amounts daily from industrial plants to commercial businesses such as markets and restaurants, as well as from farm crops to residential sector. Instances of common biomass residues are given by sawdust, spent coffee grounds, sugarcane bagasse, rice husks, poultry litter and fruit peels. Decentralized generation of wastes is an obstacle to its reuse because collection costs often outweigh reuse profits for such inexpensive and difficult-to-handle bulk solids. On the other hand, wastes generation is centralized in industries which allows for in-situ processing of biomass wastes into fuels or renewable energy to improve companies' energy balance and reduce their carbon footprint (McKendry, 2002; Perea-Moreno et al., 2019).

Fuels and renewable energy generation is directly related to efficient injection of biomass particles into reactors producing a good penetration and mixing. This task is quite challenging due to variations in samples' particle-size distribution, shape, and moisture content. Such variations might worsen samples' flowability thus increasing its likelihood to clog feeders or result in unstable flow (Ramírez-Gómez, 2016; Ilic et al., 2018). Biomass feeding to reactors might be performed under batch, semi-continuous or continuous mode using mechanical or non-mechanical feeding devices with associated pros and cons (Berruti et al., 2009; Dai and Grace, 2011; Dai et al., 2012; Woodruff et al., 2012; Massaro Sousa and Ferreira, 2020b, 2020a; Bai and Si, 2021; Gomes et al., 2021).

Recently, the hydrodynamics of a horizontal pressurized injector for feeding sawdust powders (mean diameter from 447 to 1,130  $\mu\text{m}$ ) into fluidized beds has been experimentally investigated with a high-speed camera (Massaro Sousa et al., 2021). The feeder showed stable and wide range of operation, with solids mass flux ranging from 60 to 450  $\text{kg}/\text{m}^2$  representing relevant conditions for solid pneumatic injection into fluidized beds. Given the available experimental data, validation of numerical models based on computational fluid dynamics and

the development of scale-up rules is of great interest for advancing the state of the art for this injector.

The commercial software CPFD Barracuda<sup>®</sup> implemented the multiphase particle-in-cell approach (MP-PIC) to solve motion equations for gas/particles flow, and it is gaining interest particularly because samples' particle-size distribution can be fully added and the simulations are solved in a time-effective way. Equipment from bench-to-industrial scale have been already simulated with this software for a wide range of applications, such as FCC regenerators, fluidized beds under different regimes, coal gasifiers, chemical looping combustors, pneumatic conveyors, etc (Chen et al., 2013; Amblard et al., 2015; Fotovat et al., 2015; Solnordal et al., 2015; Ariyaratne et al., 2017; Chladek et al., 2018; Kraft et al., 2018; Tu and Wang, 2018; Bandara et al., 2021; Pal and Theuerkauf, 2021; Sung et al., 2021).

This paper presents the simulation of the mentioned pressurized gas injector with sawdust powders using the CFD MP-PIC approach implemented in the Barracuda commercial code. To the best of author's knowledge, this is the first simulative study addressing this type of non-mechanical feeder, which deals with a fast release of pressurized gas to transport and inject biomass powders into fluidized beds. First, the numerical model is compared with experimental data and the effect of some model inputs on system's hydrodynamics is discussed. Finally, the resulting model is used to extrapolate the feeder behavior at different operating and design conditions.

## 2 Material and Methods

### 2.1 Experimental setup and data

The system dimensions described elsewhere (Massaro Sousa et al., 2021) are shown in Fig. 1. It consists of a 0.02 m-internal diameter pipe that is divided in two sections (i.e., pressurized chamber and injection line) when the ball valve is closed. Initially, a given mass of

solids ( $M$ ) is stored at the left section that is pressurized with different gas pressures ( $P$ ). Once the ball valve is manually opened, the solids are transported to the cold-flow unit due to gas pressure release and momentum transfer. A continuous low secondary air velocity ( $U$ ) can be also added to minimize the accumulation of powders in the injection line.

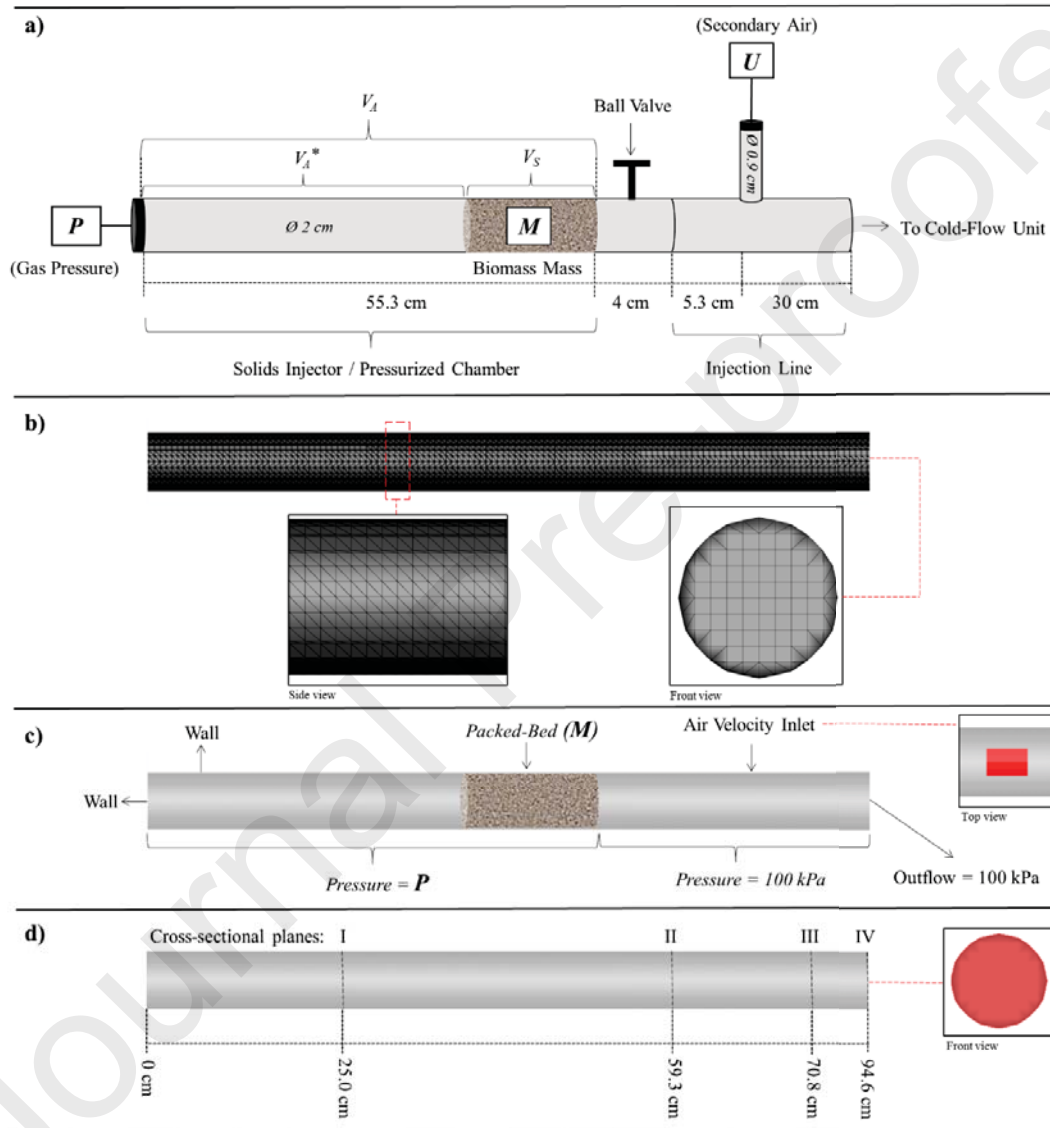


**Fig. 1.** Injection system for sawdust powders: a) experimental unit, b) geometry and mesh, c) initial and boundary conditions, d) monitored planes: I, II, III, and IV.

The gas-solid hydrodynamics in the injection line has been investigated for different operating conditions of  $P$  and  $M$ , using a high-speed camera with acquisition rate of 3,000 images/s (Massaro Sousa et al., 2021). The experimental flow time ( $t_e$ ), mean solids mass flux ( $G_S$ ) and solids flow concentration ( $\varepsilon_S$ ) determined previously are used here for numerical

model testing. Note that  $t_e$  was measured experimentally and represents the time interval for powders to be released from the pressurized chamber and settle in the injection line. Another parameter considered in model/experiments comparison is  $R$ , which represents the mass of residual sawdust in the injection line after total gas release from the pressurized chamber divided by  $M$ .

Experimental data is shown in Table 1 for eight different injection conditions, with  $P$  and  $M$  range from 300 to 500 kPa and 0.003 to 0.024 kg, respectively. The secondary superficial gas velocity ( $U$ ) was maintained at 4.4 m/s under all conditions. Note that  $V_S/V_A$  is the ratio of the initial volume of solids to the volume of the pressurized air at normal conditions in the chamber, as illustrated in Fig. 1a. This parameter impacts the solid concentration in the injection line:

$$\frac{V_S}{V_A} = \frac{M}{\left(V - \frac{M}{\rho_p}\right) \cdot \left(\frac{T_{ref}}{T}\right) \left(\frac{P}{P_{ref}}\right) \rho_p} \quad (1)$$

$$V_A = \frac{\left(V - \frac{M}{\rho_p}\right) \cdot \left(\frac{T_{ref}}{T}\right) \left(\frac{P}{P_{ref}}\right)}{V} \quad (2)$$

in which  $V$  is the volume of the pressurized chamber, equal to  $1.73\text{E-}4 \text{ m}^3$ , whereas  $T_{ref}$  and  $P_{ref}$  are 273.15 K and 101.33 kPa, respectively.

**Table 1.** Summary of the injection conditions and experimental data.

Tests	$P$ (kPa)	$M$ (kg)	$V_S/V_A$ (-)	$t_e$ (s)	$G_S$ ( $\text{kg}\cdot\text{m}^{-2}\cdot\text{s}^{-1}$ )	$\epsilon_S$ (-)	$R$ (%)
1	500	0.003	0.0036	0.045	210	0.058	0.3
2	400	0.003	0.0045	0.049	190	0.065	0.7
3	300	0.003	0.0060	0.096	100	0.089	3.1
4	300	0.006	0.0122	0.134	138	0.103	2.7
5	500	0.012	0.0152	0.134	284	0.113	0.9
6	400	0.012	0.0190	0.147	254	0.123	2.6
7	300	0.012	0.0253	0.167	216	0.137	5.6
8	500	0.024	0.0328	0.212	350	0.157	2.9

## 2.2 Injector geometry and mesh

The injector geometry was built in Catia V5<sup>®</sup> with the same dimensions of the experimental feeder. The mesh was generated directly on the simulation software, Barracuda Virtual Reactor<sup>®</sup> 21.0, mainly with cubic cells except for a few that are cut by the walls, as shown in Fig. 1b. The ball valve and secondary air inlet are considered in the simulations through boundary conditions as given in Fig. 1c.

A mesh refinement study was conducted in one condition (Test 5) as presented in Fig. 2. The solids flux and simulation time ( $t^*$ ) for different mesh refinement ( $N$ ) are presented. While the simulation time increases up to 23 times from coarse to fine mesh, the solids flux shows a weak dependence with  $N$ , as  $G_S$  increases only about 15% in the same interval. Thus, to achieve a compromise between simulation time and accuracy, 48,100 cells was selected for simulating the 2-cm diameter solids injector. This compromise allows also to use similar cell sizes for the simulation of larger injector geometries as presented later in this paper. The selected mesh corresponds to a cell density of 162 cells/cm<sup>3</sup> considering that the total geometry volume is 2.97E-4 m<sup>3</sup>.

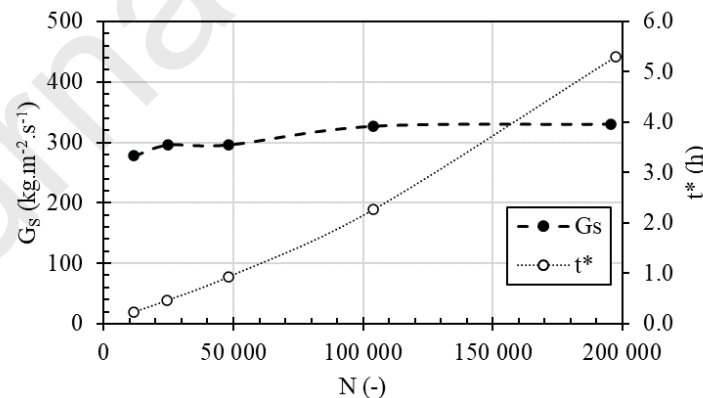


**Fig. 2.** Solids flux ( $G_S$ ) and simulation time ( $t^*$ ) as a function of number of cells ( $N$ ).  $P$  and  $M$  are set as in test 5.

## 2.3 Numerical model

The multiphase particle-in-cell (MP-PIC) method consists in using a hybrid Eulerian/Lagrangian approach to solve mass and momentum balances for gas and particles, as

described below (Andrews and O'Rourke, 1996; Snider, 2001). The gas phase is treated as a continuum in a Eulerian framework by solving the averaged Navier-Stokes equations for mass and momentum:

$$\frac{\partial(\alpha_g \rho_g)}{\partial t} + \nabla \cdot (\alpha_g \rho_g \vec{u}_g) = 0 \quad (3)$$

$$\frac{\partial(\alpha_g \rho_g \vec{u}_g)}{\partial t} + \nabla \cdot (\alpha_g \rho_g \vec{u}_g \vec{u}_g) = -\alpha_g \nabla P + \alpha_g \rho_g \vec{g} + \nabla \tau_g - F \quad (4)$$

in which  $\alpha_g, \rho_g, \vec{u}_g$  are the volume fraction, density, and velocity of the gas, respectively, while  $\nabla P$  is the pressure gradient in the system. The gas stress tensor ( $\tau_g$ ) is shown in Eq. (5), while  $F$  represents the momentum exchange rate between gas and solid phase.

$$\tau_g = \mu_g (\nabla \vec{u}_g + \nabla^T \vec{u}_g) - \frac{2}{3} \mu_g \nabla \cdot \vec{u}_g \vec{I} \quad (5)$$

Particles are treated with a hybrid Eulerian-Lagrangian approach where the mass and momentum balances for the solid phase are given by:

$$\frac{\partial(\alpha_s \rho_s)}{\partial t} + \nabla \cdot (\alpha_s \rho_s \vec{u}_s) = 0 \quad (6)$$

$$\begin{aligned} \frac{\partial(\alpha_s \rho_s \vec{u}_s)}{\partial t} + \nabla \cdot (\alpha_s \rho_s \vec{u}_s \vec{u}_s) + \nabla \tau_s + \alpha_s \nabla P = \alpha_s \rho_s \vec{g} + \iint f m_p D(\vec{u}_g - \vec{u}_p) dm_p du_p \\ - \nabla \left[ \iint f m_p (\vec{u}_p - \vec{u}_s) (\vec{u}_p - \vec{u}_s) dm_p du_p \right] \end{aligned} \quad (7)$$

in which, the mean solid velocity ( $\vec{u}_s$ ) and solid volume fraction ( $\alpha_s$ ) are defined by:

$$\vec{u}_s = \frac{1}{\alpha_s \rho_s} \iint f m_p \vec{u}_p dm_p du_p \quad (8)$$

$$\alpha_s = \iint f \frac{m_p}{\rho_s} dm_p du_p \quad (9)$$

$$\alpha_g + \alpha_s = 1 \quad (10)$$

In Eq. (7),  $f$  is the particle probability distribution (Snider, 2001) while  $D$  is the drag function. With the MP-PIC method, the particle probability distribution  $f$  is discretized into

clouds which represent a certain number of particles with same diameter, mass, and velocity. At a given simulation time  $t$ , the cloud properties are interpolated to the Eulerian grid to solve the solid phase equations. Once the equations are solved on the grid, the Eulerian grid properties such as gas velocities, gas pressure gradients and solids stress gradients are interpolated back to the clouds to update their positions and velocity using a lagrangian approach with the following equations. The position of the cloud at the next time step  $x_p^{n+1}$  is calculated with Eq. (11) where  $x_p^n$  is the cloud position at the current time step,  $\Delta t$  is the time step and  $U_p^{n+1}$  is the cloud velocity at the next time step.

$$x_p^{n+1} = x_p^n + \Delta t U_p^{n+1} \quad (11)$$

Then,  $U_p^{n+1}$  is calculated as:

$$U_p^{n+1} = \frac{U_p^n + \Delta t \left[ D U_{g,p}^{n+1} - \frac{1}{\rho_s} \nabla P_p^{n+1} + g - \frac{1}{\alpha_s \rho_s} \nabla \tau_p^{n+1} \right]}{1 + \Delta t D} \quad (12)$$

In which  $U_{g,p}^{n+1}$  is the gas velocity at  $t+\Delta t$  interpolated to the cloud position;  $P_p^{n+1}$  is the pressure at  $t+\Delta t$  interpolated to the cloud position;  $\tau_p^{n+1}$  is the solid stress at  $t+\Delta t$  interpolated to the cloud position.

One of the drag models employed in this study is based on Energy-Minimization Multi-Scale (EMMS) approach, with the following expression:

$$D = \frac{9 \mu_g}{8 \rho_p d_p^2} f_e \quad (13)$$

$$f_e = \begin{cases} \frac{1}{18\alpha_g} \left( c_0 \frac{\alpha_s}{\alpha_g} + c_1 Re \right) & \alpha_g < 0.74 \\ (c_2 + c_3 Re^{c_{15}}) \omega & \alpha_g \geq 0.74 \text{ and } Re < 1000 \\ \frac{Re}{c_4 24} \omega & \alpha_g \geq 0.74 \text{ and } Re > 1000 \end{cases} \quad (14)$$

$$\omega = \begin{cases} c_5 + \frac{c_6}{4(\alpha_g + c_7)^2 + c_8} & 0.74 \leq \alpha_g \leq 0.82 \\ & 0.82 < \alpha_g \leq 0.97 \\ & 0.97 < \alpha_g \leq 1 \end{cases} \quad (15)$$

$$c_9 + \frac{c_{10}}{4(\alpha_g + c_{11})^2 + c_{12}} \\ c_{13} + c_{14}\alpha_g$$

in which,  $c_0=150$ ,  $c_1=1.75$ ,  $c_2=1.0$ ,  $c_3=0.15$ ,  $c_4=0.44$ ,  $c_5=-0.576$ ,  $c_6=0.0214$ ,  $c_7=-0.7463$ ,  $c_8=0.0044$ ,  $c_9=-0.0101$ ,  $c_{10}=0.0038$ ,  $c_{11}=-0.7789$ ,  $c_{12}=0.0040$ ,  $c_{13}=-31.8295$ ,  $c_{14}=32.8295$ , and  $c_{15}=0.687$ . Note that the EMMS is already implemented in Barracuda and the values for the constants are based on a previous study (Yang et al., 2004).

The solid phase stress tensor ( $\tau_s$ ), also present in Eq. (7), is given by:

$$\tau_s = \frac{10P_s\alpha_s^\beta}{\max[\alpha_{s,max} - \alpha_s, \varepsilon_p(1 - \alpha_s)]} \quad (16)$$

in which  $P_s$  is a constant with units of pressure (1 Pa),  $\alpha_{s,max}$  is the solid volume fraction at close pack,  $\beta$  is a constant between 2 and 5 and a value of 3 was utilized in this study, and  $\varepsilon_p$  is a very small number ( $10^{-8}$ ). Comparatively, the modeling of the solid phase stress tensor is simpler than the one used in the kinetic theory of granular flow where a specific equation is used for the transport of the granular temperature (Lun et al., 1984; Gidaspow, 1994).

The collisions of the solid phase with walls are considered with Eq. (17). The resulting particles cloud velocity ( $\vec{u}_p$ ) following a wall impact, at the instant  $n+1$ , is decreased by normal ( $\eta_n$ ) and tangential ( $\eta_t$ ) retention parameters for momentum losses and angle of impact with respect to the vertical direction ( $\theta$ ):

$$\vec{u}_p^{n+1} = [(\eta_n - \eta_t)(1 - \cos \theta) + \eta_n] \vec{u}_p^n \quad (17)$$

## 2.4 Simulation conditions

The solid injection simulations were performed under the conditions shown in Table 1. Simulations were performed in Barracuda Virtual Reactor<sup>®</sup> 21.0 with a Linux computer (Intel<sup>®</sup> Xeon<sup>®</sup>, E5-1620 v3, 3.5 GHz) during a total simulation time of 0.3s, and with a time step of

$10^{-5}$ s. Simulating 0.3s is sufficient to cover all experimental conditions because the maximum experimental flow time is 0.212s (test 8).

The initial and boundary conditions are depicted in Fig. 1c. A given mass of sawdust powders ( $M$ ) is initially packed in the solids injector, at the same location as experimentally, while the gas phase is pressurized at a given  $P$  in the chamber region. The pressure on the injection line and ball valve regions are set as 100 kPa (atmospheric pressure), and outflow for gas and solids is set at the boundary of the cold-flow unit also with 100 kPa. A secondary air velocity ( $U$ ) of 4.4 m/s is added perpendicularly to the injection line through a square plane of equal area than the experimental inlet. Finally, a wall boundary condition is set on the left end of the pressurized chamber.

Some planes were created in the geometry to monitor the gas-solid flow, as shown in Fig. 1d, such as planes I, II, III, and IV. Flow data was acquired every  $10^{-4}$ s to fully capture the gas-solid hydrodynamics in the injection line, which physically corresponds to a fast transport of bulk solids by pressurized gas release. Note that the region between planes II and III corresponds to the same location that the gas-solid flow was assessed experimentally with the high-speed camera (Massaro Sousa et al., 2021).

In the simulations, mean values for  $G_S$  and  $\varepsilon_s$  were obtained considering the positions and experimental data acquisition methods (Massaro Sousa et al., 2021). Thus, the solids mass flux passing through plane III was monitored and integrated until 99.5% of the cumulative mass curve is reached ( $M_{99.5\%}$ ). The corresponding flow time  $t_{99.5\%}$  provides the  $G_S$  as:

$$G_S = \left( \frac{M_{99.5\%}}{A \cdot t_{99.5\%}} \right) \quad (18)$$

in which  $A$  is the cross-sectional area of the injection line of  $3.14\text{E-}4$  m<sup>2</sup>. The mean solids fraction is obtained iteratively by Eq. (19), which is the same equation used to average the

experimental results. Note that  $\varepsilon_S$  calculated from Eq. (19) is a volumetric ratio which agrees with the solids fraction definition:

$$\varepsilon_S = \frac{Q_S}{Q_t + Q_S} = \frac{\frac{G_S A}{\rho_p \varepsilon_S}}{Q_t + \frac{G_S A}{\rho_p \varepsilon_S}} \quad (19)$$

in which  $Q_t$  is the volumetric gas flowrate in plane III averaged until  $t_{99.5\%}$ . We have also verified that using Eq. (19) is consistent with the cross-sectional mass-weighted average  $\varepsilon_S$  gathered from the simulations. Finally,  $R$  is calculated by dividing the mass of solids accumulated in the injection line at the end of simulation by  $M$ .

The drag model used was based on the Energy-Minimization Multi-Scale (EMMS), and the normal ( $\eta_n$ ) and tangent-to-wall ( $\eta_t$ ) parameters were set as 0.70. A detailed study about these parameters is presented in Sections 3.1 and 3.2, respectively. Other variables have been maintained as Barracuda's default, such as: close pack volume fraction of 0.60, diffuse bounce of 5, and particle-particle interactions ( $P_s=1$  Pa,  $\beta=3$ ,  $\varepsilon_p=10^{-8}$ ,  $m=40\%$ ).

## 2.5 Sawdust properties

The particle size distribution of the sawdust sample is shown in Fig. 3 with  $d_{50}$  of 647  $\mu\text{m}$ . The cumulative curve has been fully inserted in the simulations along with the particle density of 1,030  $\text{kg/m}^3$  (Geldart B), and initial particle volume fraction of 0.21 (averaged between loose and tapped conditions). Note that the particle volume fraction of sawdust is within the range of typical values for other biomass particles, generally from 0.07 to 0.30, as reported in the literature (Tannous et al., 2013; Dhiman et al., 2016; Massaro Sousa and Ferreira, 2019). The methods for sample characterization are presented in detail elsewhere (Massaro Sousa et al., 2021). The particle shape factor was considered as 1 in the simulations.

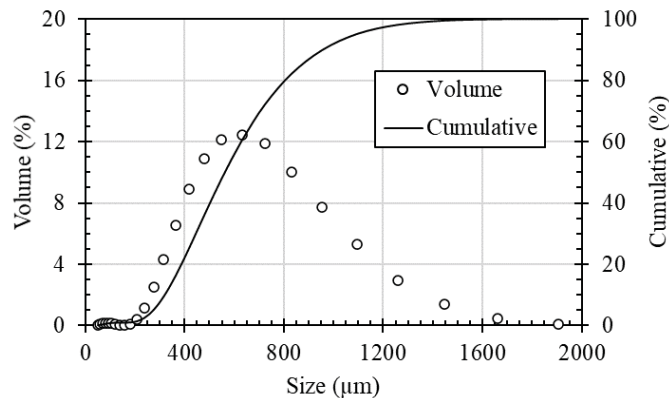


Fig. 3. Particle size distribution for the sawdust sample with  $d_{10}$ ,  $d_{50}$ , and  $d_{90}$  equal to 370, 647, and 1,100  $\mu\text{m}$ .

### 3 Results and Discussion

#### 3.1 Effect of the drag model

In the following sections, the influence of the drag model and particle-to-wall interactions are investigated to find the best set that represents the experiments. To minimize the number of simulations, the parameters' effect were studied under operational settings of test 5 (Table 2), however similar effects are expected under conditions of tests 1-8.

Different drag models have been evaluated to predict the horizontal transport of sawdust from the injector, consisting of Gidaspow (GD), Turton-Levenspiel (TL), Haider-Levenspiel (HL), and Energy-Minimization Multi-Scale (EMMS). These drag models are already implemented in Barracuda Virtual Reactor<sup>®</sup> 21.0 and commonly used for gas-solid flows (Turton and Levenspiel, 1986; Haider and Levenspiel, 1989; Gidaspow, 1994; Yang et al., 2004; Chen et al., 2013).

In Fig. 4, simulation results for solids mass flux matches experimental data (white bar) accurately with the EMMS drag model, whereas the other homogeneous drag models overestimated the solids flux by 6 to 9 times. Thus, the EMMS has been selected for the simulations of this work. Previous MP-PIC studies have also demonstrated improved hydrodynamics predictions with the EMMS method, while overestimation of fluidization patterns were observed with the other drag models for circulating fluidized beds with Geldart

B and D (Kraft et al., 2017; Kraft et al., 2018; Tu and Wang, 2018) and fluidized beds with Geldart A (Feng et al., 2018). A recent MP-PIC study on pneumatic conveying of drill cuttings ( $d_{50}=290 \mu\text{m}$ ,  $\rho_p=2,715 \text{ kg/m}^3$ , Geldart B) used the Gidaspow drag model multiplied by 0.50 to reduce the drag force and match the pressure drop and particle velocity in their pipeline (Sung et al., 2021).

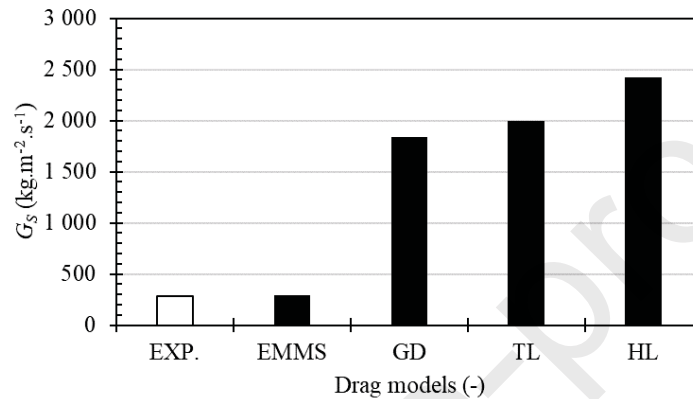


**Fig. 4.** Solids flux ( $G_s$ ) for various drag models with  $P$  and  $M$  set as in test 5.

### 3.2 Effect of particle-to-wall collision

Particle-to-wall interactions are addressed in Barracuda<sup>®</sup> with two main parameters, accounting for normal ( $\eta_n$ ) and tangent ( $\eta_t$ ) collisions with the wall. A value of 1.0 indicates a perfectly elastic collision, which means that the particle bounce back from or slide tangent to the wall with the same momentum before the contact, whereas 0.0 indicates that the momentum is entirely dissipated. Information about such parameters are difficult to be obtained experimentally, thus different values have been numerically investigated from 0.85 to 0.10, and its effect on the injector dynamics are presented in Fig. 5. Since both parameters are unknown, we used the same values for  $\eta_n$  and  $\eta_t$  while analysing their effect on the responses.

The cumulative mass of sawdust passing through plane III ( $M^*$ ) is shown in Fig. 5a during 0.3s of simulation for different  $\eta_n$  and  $\eta_t$ . The shape of the curves are similar among each other, with an initial fast transport of solids followed by an asymptotical pattern due to the decrease of the pressurized chamber gas, which is the driving force for the transport of solids. Besides,

curves become less inclined as parameters values decreases to 0.10, indicating that the mean solids mass flux decreases by decreasing  $\eta_n$  and  $\eta_t$ . For example,  $G_S$  decrease by 11% from 0.85 to 0.10. Moreover, as shown in Fig. 5b, there is a significative increase in the accumulation of sawdust in the injection line ( $R$ ), from 0.2 to 12.3%, by decreasing  $\eta_n$  and  $\eta_t$  from 0.85 to 0.10 which is due to higher friction among the particles and wall.

These results are in agreement with the expected behavior, since enhanced loss of momentum occurs with lower parameters values, hence decreasing  $G_S$  and increasing  $R$ . For the simulation of the solids injector with sawdust,  $\eta_n$  and  $\eta_t$  have been fixed at 0.70 to match experimental data for test 5 ( $R$  and  $G_S$ ). Note that 0.70 is within the range of recommended values in Barracuda's manual, as typical parameters values of 0.50 and 0.85 are used for soft and hard particles, respectively.

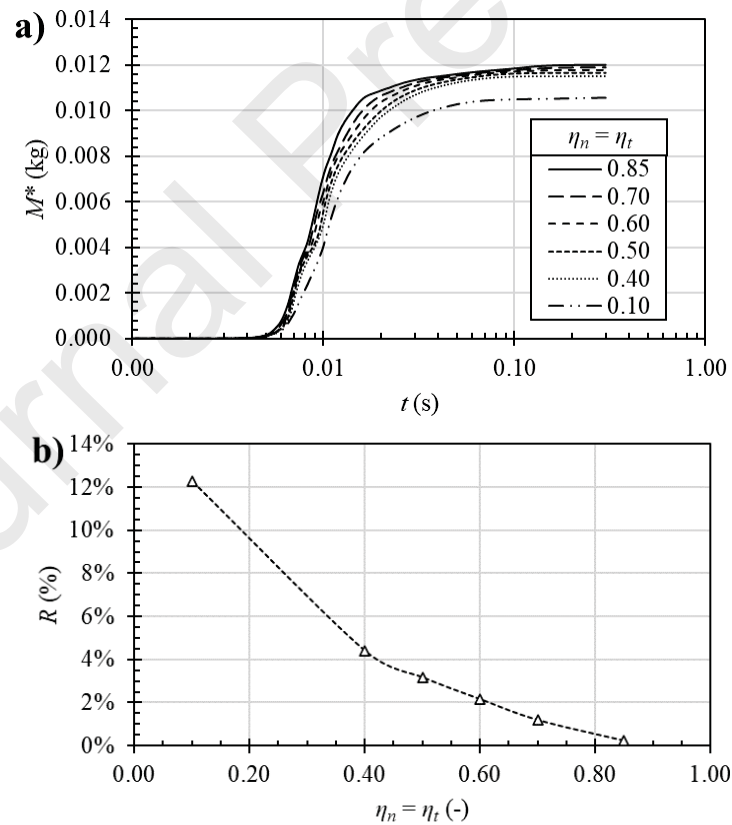


**Fig. 5.** Simulated results for different  $\eta_n$  and  $\eta_t$ : a) sawdust mass passing through plane III ( $M^*$ ), and b) accumulation of powders in the injection line ( $R$ ).  $P$  and  $M$  are set as in test 5.

### 3.3 Numerical model testing

In this section, the numerical model is tested under different operating conditions, tests 1 to 8 (Table 1). A consistent quantitative agreement between simulated and experimental data is presented in Fig. 6, in terms of solids mass flux, flow time, and flow concentration. On average, relative deviations were lower than 14, 11, and 2% for  $G_S$ ,  $\varepsilon$ , and  $t_e$ , respectively, from tests 1 to 8 ( $0.0036 \leq V_S/V_A \leq 0.0328$ ). The relative deviations were calculated as the difference between simulated and experimental values divided by the experimental one.

As demonstrated experimentally (Massaro Sousa et al., 2021), depending on the initial settings for  $M$  and  $P$ , different solids mass flux and flow concentrations can be obtained in the injection line. The numerical model accurately reproduced such behaviors from tests 1-8. Under stable operating conditions, higher solids mass fluxes are obtained by using higher gas pressure and/or initial mass of solids in the injector.

Fig. 6a presents the trends of simulation data under decreasing  $P$  (points 1 to 3, and 5 to 7) or increasing  $M$  (points 3 to 4, and 7 to 8) for different  $V_S/V_A$  values. The qualitative experimental behavior was reproduced extremely well by the simulations, specially for  $0.005 \leq V_S/V_A \leq 0.020$  with relative deviations of 5% (within the experimental error bars). Outside of this range, the deviations reached up to 20%, possibly because the pulse injections were either more dilute or dense compared to the conditions of test 5 ( $V_S/V_A=0.0152$ ), which was used for selecting the drag model and particle-wall parameters.

Moreover, it was observed experimentally that both flow time and solids concentration in the injection line increase as  $V_S/V_A$  increases (i.e., with increasing initial solids ratio in the injector), and the numerical model also predicts it as presented in Figs. 6b and 6c.

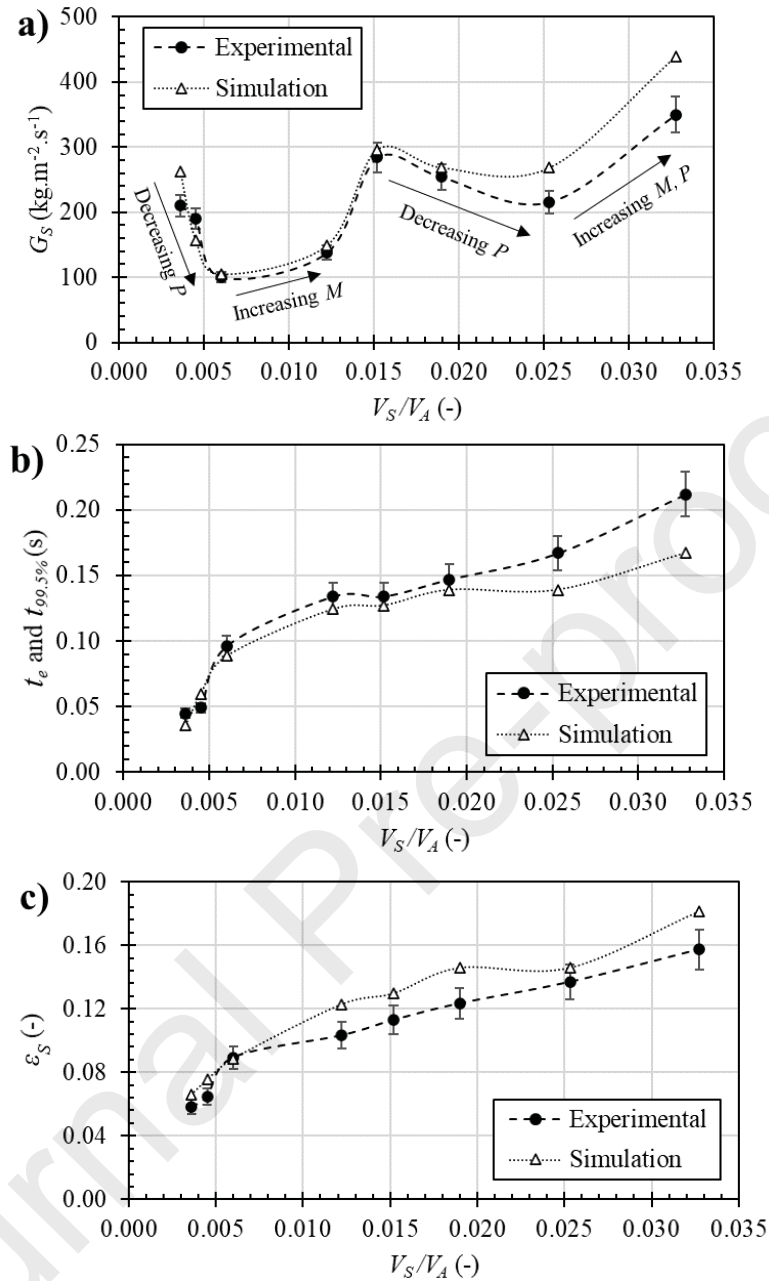


**Fig. 6.** Experimental and simulated data for a)  $G_S$ , b)  $t_e$  and  $t_{99.5\%}$ , and c)  $\varepsilon_S$ .

### 3.4 Contours for solid and gas phases

The transient behavior for the injection of sawdust powders is illustrated in Fig. 7 under test 5 conditions. The discrete phase is coloured according to the particle velocity, from 0 to 80 m/s, while the continuous phase is painted in terms of gas pressure, from 100 to 500 kPa, as it is the driving force for the solids transport. At  $t=0\text{s}$ , the particles are at rest and the gas is pressurized in the chamber with  $P=500$  kPa.

As soon as the simulation starts, the gas is released downstream with  $P$  dropping rapidly to 400, 300, and 200 kPa in 0.009s, as shown in Figs. 7b to 7d, respectively. In this interval, the solids are accelerated by transfer of gas momentum, and there is a distribution of particle velocities and concentrations along the geometry. At the injection line section, there is initially a dilute transport of solids at high-speed (Fig. 7b), followed by a more dense flow with velocity from 30 to 80 m/s (Figs. 7c to 7d). On the other hand, at the pressurized chamber region the solids velocity are generally lower than 30 m/s. These features are in line with experimental observations with a high-speed camera at 3,000 frames per second (Massaro Sousa et al., 2021).

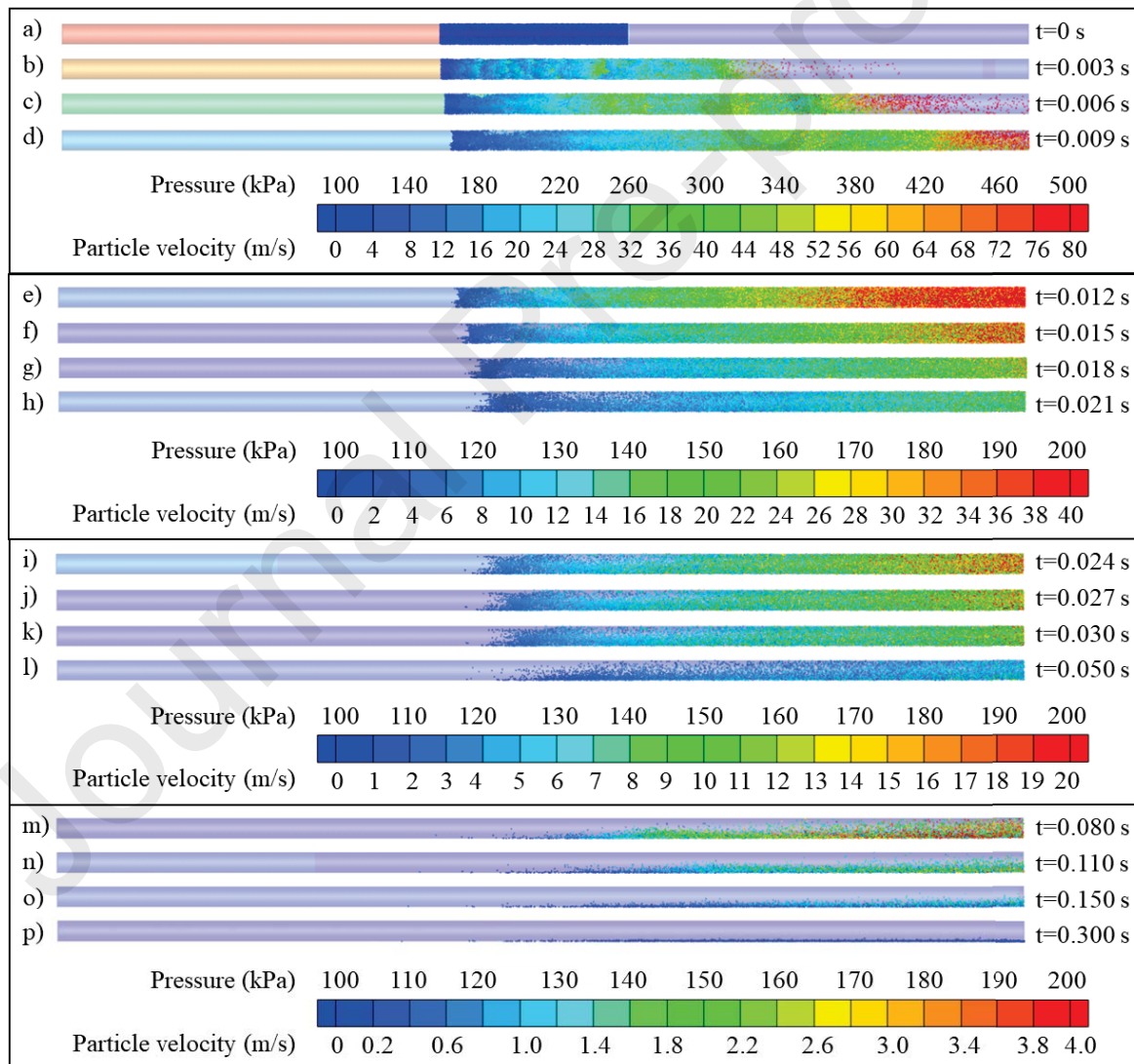


**Fig. 7.** Counters for particles velocity (discrete phase colour) and gas pressure (background colour) at different times.  $P$  and  $M$  are set as in test 5.

In the images, the coloring scale range has been reduced to better assess the phenomena. From Fig. 7e and onwards, a decelerating flow of solids is verified due to a combined effect of pressurized gas emptying at the solids injector chamber ( $P \approx 100$  kPa) and loss of momentum by particle-particle and particle-wall collision. The solids are homogeneously distributed along injection's line diameter, until they begin to settle at the lower section of the tube (Fig. 7m), and their residual movement is due to the powder's inertia and bouncing. Finally, there is almost no transport of powders at  $t=0.3$ s, and the residual solids accumulate throughout the base of the injection line (Fig. 7p).

The transient behavior can be also visualized in Fig. 8, in which the flow concentration ( $\varepsilon_S$ ) and total interstitial gas velocity ( $U_t$ ) were averaged in the cross-sectional plane III over time, while the gas pressure was averaged in plane I (Fig. 1d). As previously described, there is a fast decrease in  $P$  due to gas release with ball valve opening, resulting in the transport of solids with peak values for  $\varepsilon_S$  up to 0.16, for total gas velocity up to 200 m/s, and for mean cross-sectional solids velocity up to 45 m/s. As  $P$  reaches atmospheric conditions, there is a deceleration pattern for  $\varepsilon_S$ ,  $U_t$  and  $U_S$  until the remaining solids settle at the injection line.

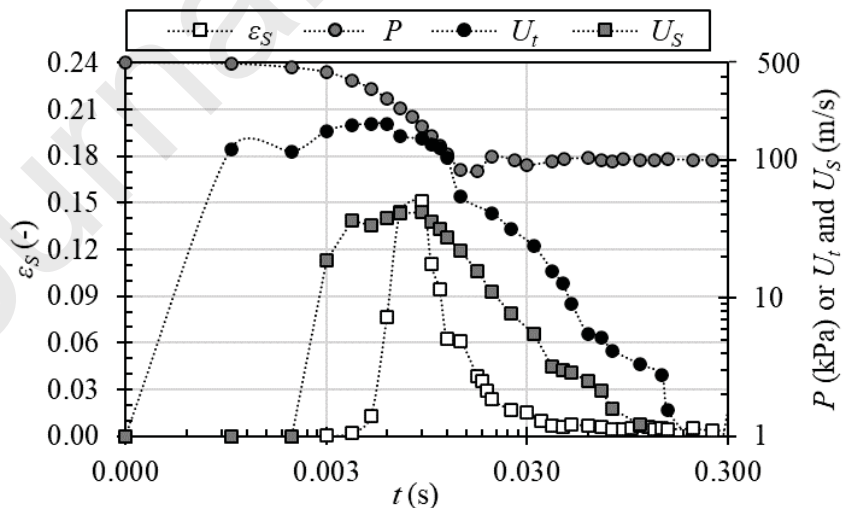


**Fig. 8.** Flow concentration ( $\varepsilon_S$ ) total interstitial gas velocity ( $U_t$ ), cross-sectional solids velocity ( $U_S$ ) and pressure ( $P$ ) over time for conditions of test 5.

### 3.5 Model extrapolation: feeder operation map

It is interesting to investigate model's responses outside of the interval that has been tested against experimental data, particularly for operating conditions that are difficult or dangerous to be implemented experimentally. Therefore, higher gas pressures are analyzed here up to 1,650 kPa, which represents a 3.3-fold increase compared to the maximum one used in the experiments ( $P=500$  kPa) (Massaro Sousa et al., 2021). The injector dimensions were maintained as shown in Fig. 1a, which means that, at maximum, 0.0364 kg of sawdust can be inserted into the pressurized chamber region.

The simulations were performed under three solids loading conditions,  $V_S/V_A$  of 0.015, 0.025, and 0.035. The solids mass flux is shown in Fig. 9a as a function of the gas pressure. The trend of the curves are similar, with an initial linear increase of  $G_S$  as  $P$  increases, until it reaches a maximum value, followed by a decreasing trend for  $G_S$ . For example, with the solids loading of 0.015,  $G_S$  can be adjusted from 100 to 650 kg/m<sup>2</sup>s by increasing  $P$  up to 1,650 kPa.

In Fig. 9b,  $G_S$  is plotted as a function of  $V_A$  that is a dimensionless parameter related to the amount of pressurized air representing the driving force for the solids transport with this injector. The curves behavior are similar to the ones described in Fig. 9a, however with the advantage that the dimensionless parameters ( $V_A$  and  $V_S/V_A$ ) are dissociated from specific experimental conditions resulting in a more general description of the phenomena. Note that these parameters can be easily calculated before any injection of solids (i.e., from initial  $P$  and  $M$  conditions) with Eqs (1) and (2).

To explain the maximum of  $G_S$  in the curves, three points have been highlighted in Fig. 9b and are illustrated in Fig. 9d. These points are under the same  $V_S/V_A$  ratio with increasing  $V_A$ , hence more solids are present in the pressurized chamber from points (1) to (3). As also, observed experimentally, a large amount of solids in the pressurized chamber provides a significant length that requires higher amount of gas for solids transport compared to when a

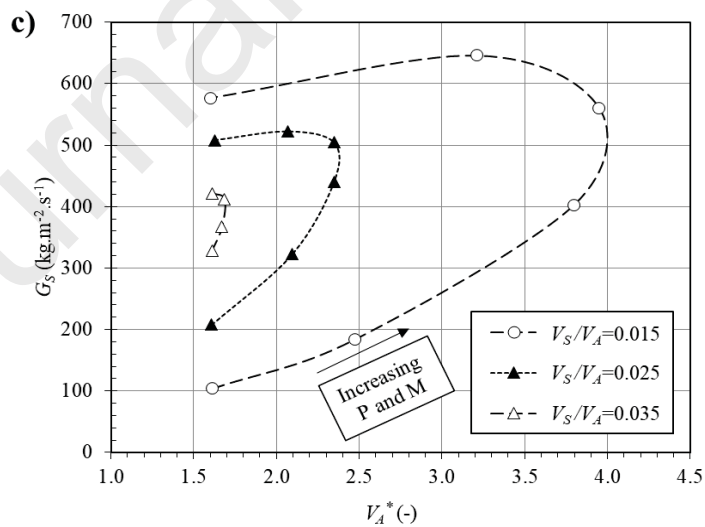
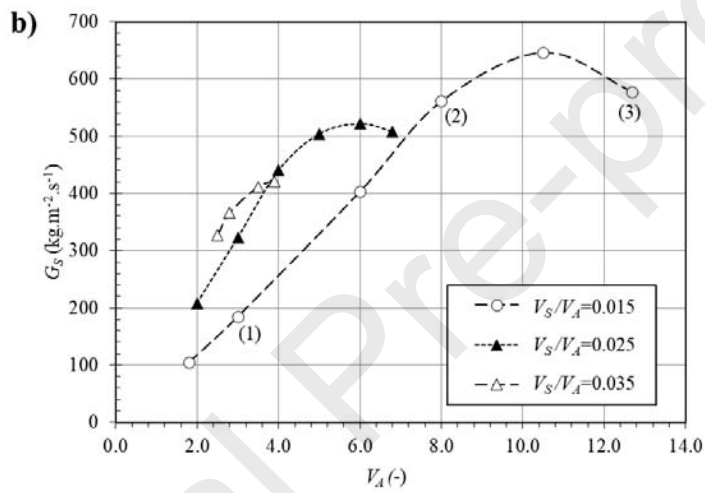
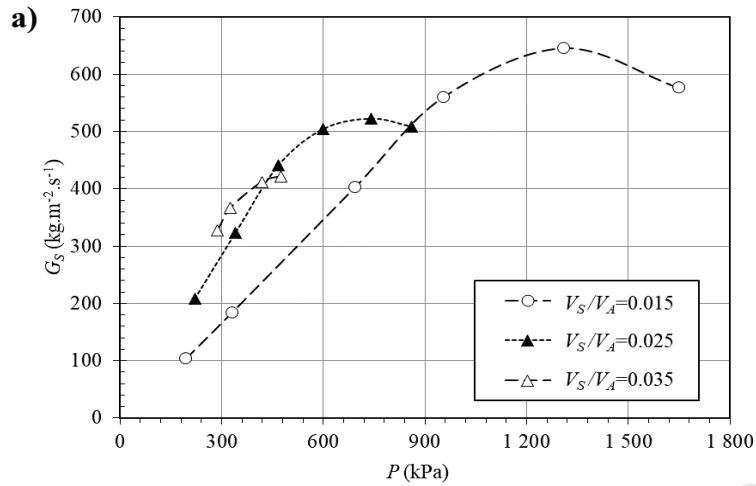
smaller portion of the chamber is occupied. However, as shown in Fig. 9d, this additional gas is limited because the pressurized chamber length is fixed, then there is a decrease in  $G_S$  as the chamber approaches its maximum powder filling limit.

The phenomena described in the previous paragraph, results that, if there is not a significant amount of pressurized gas available on the left side of the packed bed (in the pressurized chamber) to push the powders ensemble, then the feeders performance is jeopardized, which means that there is a decrease in  $G_S$  and significative accumulation of solids in the injection line (e.g.,  $R > 10\%$ ) (Massaro Sousa et al., 2021). There is a dimensionless parameter,  $V_A^*$ , that captures the portion of air pressurized on the left side of the packed bed, as illustrated in Fig. 9d. It is calculated by considering the mean bulk density between loose and tapped conditions ( $\rho_m$  of 215 kg/m<sup>3</sup>):

$$V_A^* = \frac{\left(V - \frac{M}{\rho_m}\right) \cdot \left(\frac{T_{ref}}{T}\right) \left(\frac{P}{P_{ref}}\right)}{V} \quad (20)$$

Experimentally the feeder malfunction occurred for  $V_A^* \leq 1.4$ , thus the simulations were performed here considering  $V_A^* = 1.6$  as the operating limit. The  $G_S$  curve plotted as a function of  $V_A^*$  is presented in Fig. 9c for the studied  $V_S/V_A$ , showing the curve inversion pattern (maximum  $G_S$  point) as a consequence of increasing solids loading in the injector.

Another remark on the operation map (Fig. 9c) is that for a given  $V_A$ , the higher the initial solids inventory ( $V_S/V_A$ ) the higher  $G_S$  because the injection of sawdust occurs in a more dense condition as was the case experimentally. This is highlighted in Fig. 9e by the mean flow concentration from 0.12 to 0.20, in the interval of  $0.015 \leq V_S/V_A \leq 0.035$ . Ultimately, Figs. 9b and 9e are useful for estimating  $G_S$  and  $\varepsilon_S$  for the actual injector by interpolating the curves, which are valid for a broad range of conditions (i.e.,  $0.015 \leq V_S/V_A \leq 0.035$ , and  $1.8 \leq V_A \leq 12.7$ , with the restritive condition that  $V_A^* \geq 1.6$ ), at least according to the simulations.



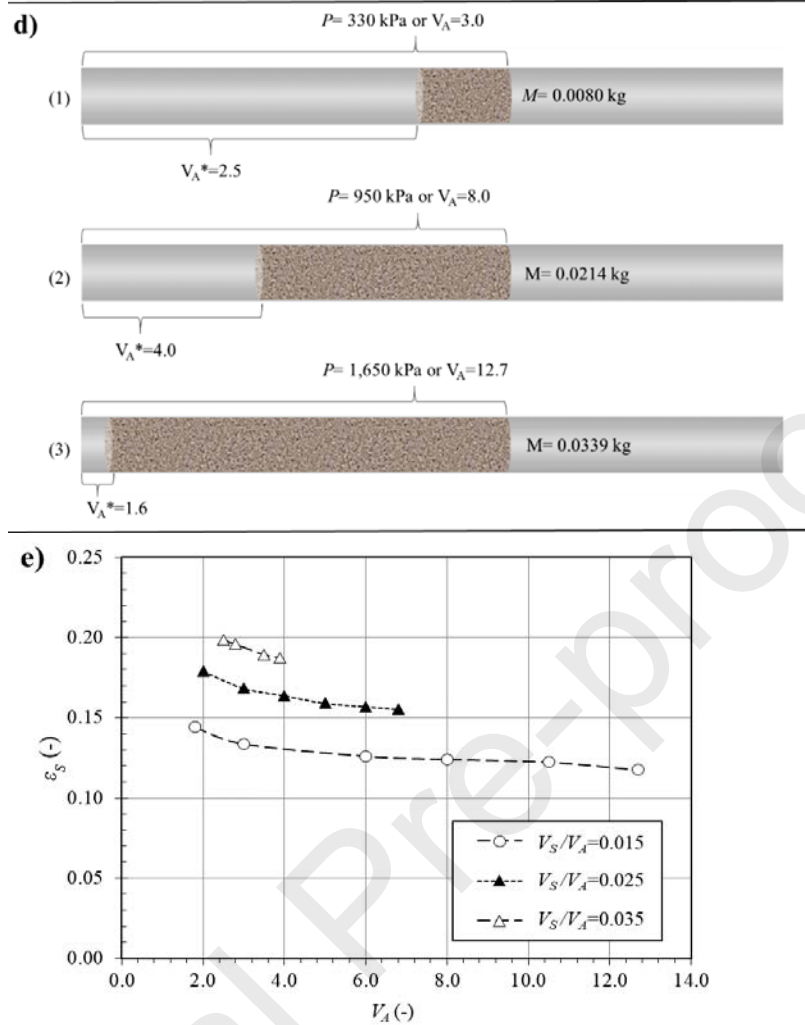


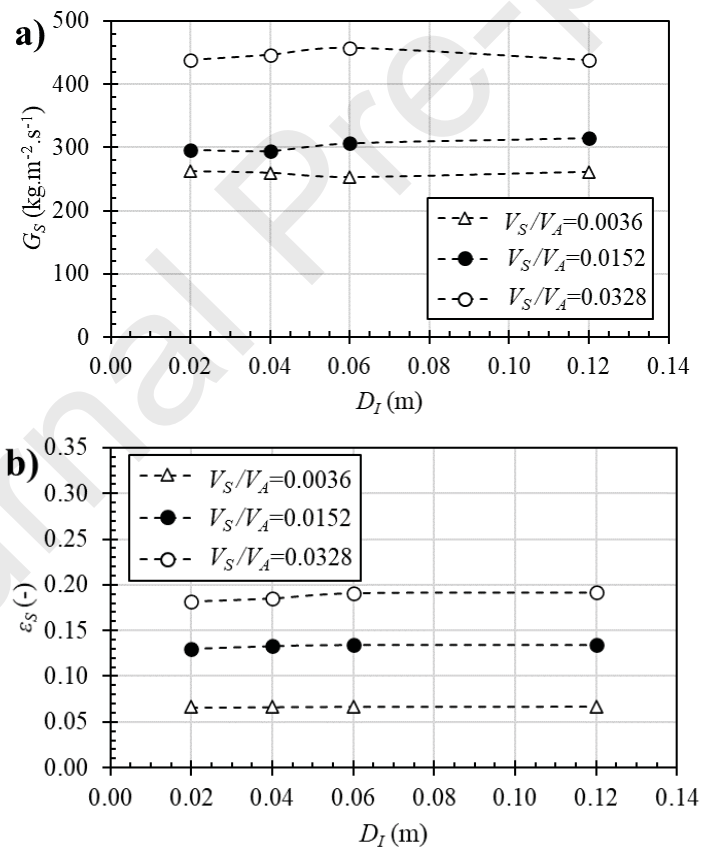
**Fig. 9.** Solids mass flux as a function of a)  $P$ , b)  $V_A$ , and c)  $V_A^*$ , as well as d) initial settings for marked points (1) to (3) with  $V_S/V_A=0.015$  and e) solids flow concentration versus  $V_A$ .

### 3.6 Model extrapolation: effect of the injector diameter

In this section, the numerical model is used to simulate injectors with larger internal diameters aiming at evaluating feeders for larger scale applications in a cost-effective way. Three different operating conditions were tested to cover dilute to dense injections, with  $V_S/V_A$  of 0.0036 (test 1), 0.0152 (test 5), and 0.0328 (test 8). The simulation setup and the cell size is equal to that validated in Section 3.3, however the initial condition for solids and gas were adjusted to match the same  $V_S/V_A$  ratio since the injector volume increases with increasing  $D$ . Thus, the gas pressure in the pressurized chamber was maintained at 500 kPa, equal to tests 1,

5, and 8 (Table 1), whereas the initial mass of solids was increased to meet similar  $V_S/V_A$ . It means that batch injections of sawdust were performed from 0.003 to 0.890 kg.

The results for mean solids flux and flow concentration are presented in Fig. 10a and 10b, respectively, for diameters from 0.02 to 0.12 m, with the latter representing a 6-fold increase of this parameter. Similar values for  $G_S$  and  $\varepsilon_S$  are observed in the range of  $0.02 \leq D_I \leq 0.12$  m, for all different initial conditions of  $V_S/V_A$ . It indicates, at least according to these simulations, that wall effects are not predominant to jeopardize the performance of this injector for  $D_I \geq 0.02$  m, providing an important conclusion for developing scale-up and operation rules for this solids injector. Ultimately, the operation map shown previously (Fig 9b and 9c) might also be employed for estimating  $G_S$  for injectors with  $D_I \geq 0.02$  m.



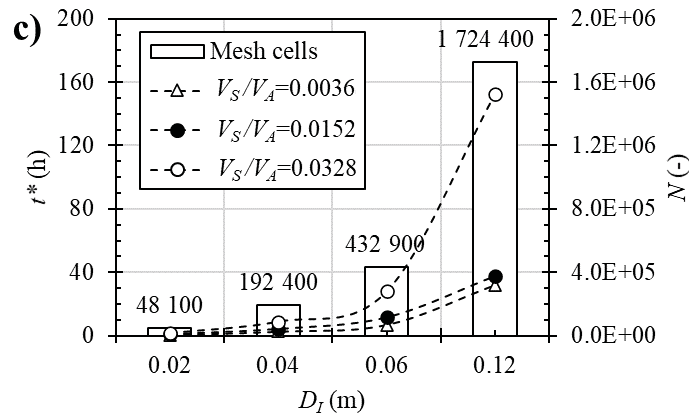


**Fig. 10.** Results for different injector diameters ( $D_I$ ), in terms of a) solids mass flux ( $G_S$ ), b) solids flow concentration ( $\epsilon_S$ ), and c) simulation time ( $t^*$ ) and number of cells ( $N$ ).

In Fig. 10c, the simulation time ( $t^*$ ) and number of cells are presented for different  $D_I$  and  $V_S/V_A$ . There is an exponential increase in  $t^*$  with increasing  $D_I$  because the mesh cells in the geometry also increases exponentially. The same mesh density of 162 cells/cm<sup>3</sup> (i.e., same cells size) has been used in the simulations to prevent mesh-related uncertainties in the calculations. Moreover, for implementation purposes, it is important to highlight that simulations with greater initial quantity of solids (i.e., those with higher  $V_S/V_A$ ) demand more time to be finished with the Barracuda software because of the higher number of clouds to track. For example, in our case, the simulations with  $V_S/V_A$  of 0.0328 takes from 2.5 to 4.8 times more time to finish than those with  $V_S/V_A$  of 0.0036.

#### 4 Conclusions

In this study, the applicability of a commercial CFD code with the MP-PIC approach is demonstrated to simulate the transport of biomass with a pressurized gas feeder. After testing against experimental data, the numerical model is used to simulate various operation conditions ( $P$  and  $M$ ), and to study the system transient hydrodynamics. The model is then extrapolated, and an operation map is build-up for the injector as a function of dimensionless parameters related to the initial solids loading and driving force intensity ( $V_S/V_A$  and  $V_A$ ). The model is also

extrapolated to study the influence of the injector diameter ( $D_I$ ) which is a key parameter for injector's scale-up.

The experimental results were accurately reproduced after some investigations on the drag law and particle-to-wall parameters. The drag law was more important to tune  $G_S$  while the particle-wall interactions affected the accumulation of powders in the injection line ( $R$ ). The solid-stress tensor function used in Barracuda, Eq. (16), is notably simpler than the set of equations employed by the kinetic theory of granular flow. Thus, careful analysis should be performed to assess the suitability of Eq. (16) to different applications, particularly for dense systems. The nature of the multiphase flow analyzed here, consisting of a dilute batch flow of solids ( $\varepsilon_S < 0.20$ ) may have contributed to some extent to the good model predictions.

In terms of the simulation results, the model has been extrapolated to different conditions of gas pressures and injector diameters in Sections 3.5 and 3.6. An assessment of the deviations of these predictions should be performed in the future with the availability of experimental data.

Future studies could simulate this solids injector with powders of different properties (particle density and size distribution) to cover other applications. Besides, further investigations could focus on validating the model for predicting gas-solid jet penetration in fixed and fluidized beds with this injector.

## 5 Nomenclature

$A$	Cross-sectional area of the injection line ( $\text{m}^2$ )
$c_0$ to $c_{15}$	Drag function constants (-)
$D$	Drag function (-)
$D_I$	Injector diameter (m)
$d_p$	Particle diameter (m)
$d_{10}$	Volumetric diameter for 10% of samples' particle-size ( $\mu\text{m}$ )
$d_{50}$	Volumetric diameter for 50% of samples' particle-size ( $\mu\text{m}$ )
$d_{90}$	Volumetric diameter for 90% of samples' particle-size ( $\mu\text{m}$ )
$F$	Gas-solid momentum exchange rate (kPa)
$f$	Particle probability distribution
$f_e$	Drag function parameter (-)
$\vec{g}$	Gravity acceleration ( $\text{m}\cdot\text{s}^{-2}$ )

$G_S$		Solids mass flux ( $\text{kg}\cdot\text{m}^{-2}\cdot\text{s}^{-1}$ )
$I$		Unit tensor (-)
$M$		Initial mass of sawdust in the injector (kg)
$M_{99.5\%}$		Mass of sawdust at 99.5% of the cumulative curve in plane III (kg)
$M^*$		Cumulative mass of sawdust passing through plane III (kg)
$M$		Maximum momentum redirection from collisions (%)
$m_p$		Mass of a particle cloud (kg)
$N$		Number of mesh cells (-)
$P$		Air pressure in the injector (kPa)
$P_{ref}$		Reference air pressure (kPa)
$P_s$		Constant in Eq. (16) (kPa)
	$P_p^{n+1}$	Pressure interpolated to cloud position at instant $n+1$ (kPa)
$Q_S$		Volumetric solid flowrate ( $\text{m}^3$ )
$Q_t$		Volumetric total gas flowrate ( $\text{m}^3$ )
$R$		Mass of sawdust accumulated on the injection line (%)
$Re$		Reynolds number (-)
$T$		Time (s)
$t_e$		Experimental injection flow time (s)
$t^*$		Simulation time (h)
$t_{99.5\%}$		Simulated injection flow time (s)
$T_{ref}$		Reference air temperature (K)
$u_g$		Gas phase velocity vector ( $\text{m}\cdot\text{s}^{-1}$ )
	$U_{g,p}^{n+1}$	Gas velocity interpolated to cloud position at instant $n+1$ ( $\text{m}\cdot\text{s}^{-1}$ )
$\rightarrow$		Particle cloud velocity vector ( $\text{m}\cdot\text{s}^{-1}$ )
$\rightarrow_p$		Particle cloud velocity vector at instant $n$ ( $\text{m}\cdot\text{s}^{-1}$ )
$\rightarrow_p^n$		Particle cloud velocity vector at instant $n$ ( $\text{m}\cdot\text{s}^{-1}$ )
$\rightarrow_p^{n+1}$		Particle cloud velocity vector at instant $n+1$ ( $\text{m}\cdot\text{s}^{-1}$ )
$u_p$		Particle cloud velocity vector at instant $n+1$ ( $\text{m}\cdot\text{s}^{-1}$ )
	$U_p^{n+1}$	Particle cloud velocity vector at instant $n+1$ ( $\text{m}\cdot\text{s}^{-1}$ )
$\rightarrow$		Solid phase velocity vector ( $\text{m}\cdot\text{s}^{-1}$ )
$u_s$		Solid phase velocity vector ( $\text{m}\cdot\text{s}^{-1}$ )
$U$		Secondary air velocity ( $\text{m}\cdot\text{s}^{-1}$ )
$U_t$		Total air velocity ( $\text{m}\cdot\text{s}^{-1}$ )
$U_S$		Cross-sectional solids velocity ( $\text{m}\cdot\text{s}^{-1}$ )
$V$		Volume of the pressurized chamber ( $\text{m}^3$ )
$V_A$		Initial volume of air defined in Eq. (2) (-)
$V_A^*$		Initial volume of air defined in Eq. (20) (-)
$V_S/V_A$		Volume of solids divided by volume of air as in Eq. (1) (-)
	$x_p^n$	Cloud position at instant $n$ (m)
	$x_p^{n+1}$	Cloud position at instant $n+1$ (m)
<i>Greek letter</i>		
$\alpha_g$		Gas phase fraction (-)
$\alpha_s$		Solid phase fraction (-)
$\alpha_{s,max}$		Parameter in Eq. (16) (-)
	$\beta$	Parameter in Eq. (16) (-)
$\nabla P$		Pressure gradient in the system (kPa)
	$\Delta t$	Simulation time step (s)
$\eta_n$		Normal particle-to-wall retention parameter (-)
$\eta_t$		Tangent particle-to-wall retention parameter (-)

	$\varepsilon$	Mean air fraction in the flow (-)
$\varepsilon_S$		Mean solid fraction in the flow (-)
$\varepsilon_p$		Parameter in Eq. (16) (-)
$\mu_g$		Gas viscosity ( $\text{kg}\cdot\text{m}^{-1}\cdot\text{s}^{-1}$ )
	$\omega$	Drag function parameter (-)
$\rho_g$		Air density ( $\text{kg}\cdot\text{m}^{-3}$ )
$\rho_m$		Mean bulk density ( $\text{kg}\cdot\text{m}^{-3}$ )
$\rho_p$		Particle density ( $\text{kg}\cdot\text{m}^{-3}$ )
$\rho_s$		Solid phase density ( $\text{kg}\cdot\text{m}^{-3}$ )
$\theta$		Angle of impact particle-to-wall ( $^\circ$ )
$\tau_g$		Gas phase stress tensor (kPa)
	$\tau_p^{n+1}$	Solid stress interpolated to instant $n+1$ (kPa)
$\tau_s$		Solid phase stress tensor (kPa)

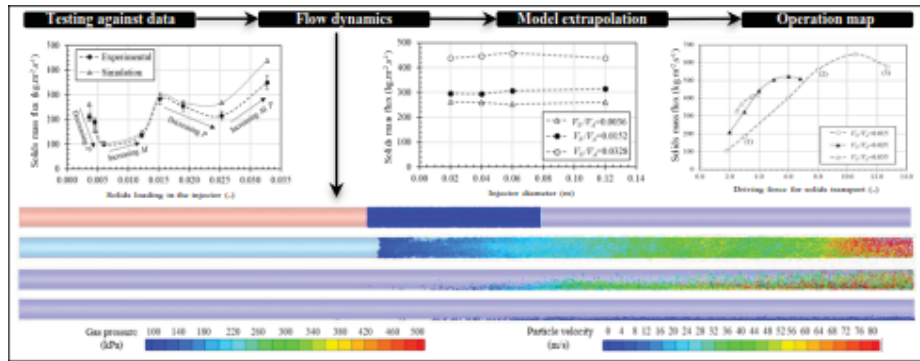
## 6 References

- Amblard, B., Bertholin, S., Bobin, C., Gauthier, T., 2015. Development of an attrition evaluation method using a Jet Cup rig. *Powder Technology* 274, 455–465. 10.1016/j.powtec.2015.01.001.
- Andrews, M.J., O'Rourke, P.J., 1996. The multiphase particle-in-cell (MP-PIC) method for dense particulate flows. *International Journal of Multiphase Flow* 22 (2), 379–402. 10.1016/0301-9322(95)00072-0.
- Ariyaratne, W.H., Ratnayake, C., Melaen, M.C., 2017. Application of the MP-PIC method for predicting pneumatic conveying characteristics of dilute phase flows. *Powder Technology* 310, 318–328. 10.1016/j.powtec.2017.01.048.
- Bai, Y., Si, H., 2021. Experimental study on feeding characteristics of conical bottom pneumatic spout feeder for biomass pyrolysis. *Chemical Engineering and Processing - Process Intensification* 166, 108490. 10.1016/j.cep.2021.108490.
- Bandara, J.C., Thapa, R., Nielsen, H.K., Moldestad, B.M.E., Eikeland, M.S., 2021. Circulating fluidized bed reactors – part 01: analyzing the effect of particle modelling parameters in computational particle fluid dynamic (CPFD) simulation with experimental validation. *Particulate Science and Technology* 39 (2), 223–236. 10.1080/02726351.2019.1697773.
- Berruti, F.M., Ferrante, L., Berruti, F., Briens, C., 2009. Optimization of an Intermittent Slug Injection System for Sawdust Biomass Pyrolysis. *International Journal of Chemical Reactor Engineering* 7 (1). 10.2202/1542-6580.2077.
- Chen, C., Werther, J., Heinrich, S., Qi, H.-Y., Hartge, E.-U., 2013. CPFD simulation of circulating fluidized bed risers. *Powder Technology* 235, 238–247. 10.1016/j.powtec.2012.10.014.
- Chladek, J., Jayarathna, C.K., Moldestad, B.M., Tokheim, L.-A., 2018. Fluidized bed classification of particles of different size and density. *Chemical Engineering Science* 177, 151–162. 10.1016/j.ces.2017.11.042.
- Dai, J., Cui, H., Grace, J.R., 2012. Biomass feeding for thermochemical reactors. *Progress in Energy and Combustion Science* 38 (5), 716–736. 10.1016/j.pecs.2012.04.002.

- Dai, J., Grace, J.R., 2011. Biomass granular screw feeding: An experimental investigation. *Biomass and Bioenergy* 35 (2), 942–955. 10.1016/j.biombioe.2010.11.026.
- Dhiman, J., Shrestha, A., Fasina, O., Adhikari, S., Via, B., Gallagher, T., 2016. Physical, ignition, and volatilization properties of biomass feedstocks dusts. *Trans. ASABE* 58, 1425–1437.
- Feng, M., Li, F., Wang, W., Li, J., 2018. Parametric study for MP-PIC simulation of bubbling fluidized beds with Geldart A particles. *Powder Technology* 328, 215–226. 10.1016/j.powtec.2018.01.024.
- Fotovát, F., Abbasi, A., Spiteri, R.J., Lasa, H. de, Chaouki, J., 2015. A CPFD model for a bubbly biomass–sand fluidized bed. *Powder Technology* 275, 39–50. 10.1016/j.powtec.2015.01.005.
- Gidaspow, D., 1994. Kinetic theory approach, in: , *Multiphase Flow and Fluidization*. Elsevier, pp. 239–296.
- Gomes, T.L., Lourenço, G.A., Ataíde, C.H., Duarte, C.R., 2021. Biomass feeding in a dilute pneumatic conveying system. *Powder Technology* 391, 321–333. 10.1016/j.powtec.2021.06.020.
- Haider, A., Levenspiel, O., 1989. Drag coefficient and terminal velocity of spherical and nonspherical particles. *Powder Technology* 58 (1), 63–70. 10.1016/0032-5910(89)80008-7.
- Ilic, D., Williams, K., Farnish, R., Webb, E., Liu, G., 2018. On the challenges facing the handling of solid biomass feedstocks. *Biofuels, Bioprod. Bioref.* 12 (2), 187–202. 10.1002/bbb.1851.
- Kraft, S., Kirnbauer, F., Hofbauer, H., 2017. CPFD simulations of an industrial-sized dual fluidized bed steam gasification system of biomass with 8 MW fuel input. *Applied Energy* 190, 408–420. 10.1016/j.apenergy.2016.12.113.
- Kraft, S., Kirnbauer, F., Hofbauer, H., 2018. Influence of drag laws on pressure and bed material recirculation rate in a cold flow model of an 8 MW dual fluidized bed system by means of CPFD. *Particuology* 36, 70–81. 10.1016/j.partic.2017.04.009.
- Lun, C.K.K., Savage, S.B., Jeffrey, D.J., Chepurniy, N., 1984. Kinetic theories for granular flow: inelastic particles in Couette flow and slightly inelastic particles in a general flowfield. *J. Fluid Mech.* 140, 223–256. 10.1017/S0022112084000586.
- Massaro Sousa, L., Amblard, B., Montjovet, F., Tebianian, S., 2021. Characterization of a pressurized feeder for biomass injection into gas-solid systems. *Chemical Engineering Research and Design* 175, 171–181. 10.1016/j.cherd.2021.08.024.
- Massaro Sousa, L., Ferreira, M.C., 2019. Spent coffee grounds as a renewable source of energy: an analysis of bulk powder flowability. *Particuology* 43, 92–100.
- Massaro Sousa, L., Ferreira, M.C., 2020a. Analysis of the performance of an L-valve feeding spent coffee ground powders into a circulating fluidized bed. *Powder Technology* 362, 759–769. 10.1016/j.powtec.2019.12.010.
- Massaro Sousa, L., Ferreira, M.C., 2020b. On the performance of a spouted bed type device for feeding spent coffee grounds to a circulating fluidized bed reactor. *Chemical Engineering Research and Design* 160, 31–38. 10.1016/j.cherd.2020.05.002.
- McKendry, P., 2002. Energy production from biomass (part 1): overview of biomass. *Bioresource Technology* 83 (1), 37–46. 10.1016/S0960-8524(01)00118-3.

- Pal, K., Theuerkauf, J., 2021. Multiphase Particle in Cell Simulations of Fluidized Beds: Studies on Bubble Rise Velocity and Minimum Fluidization Velocity. *Chemie Ingenieur Technik* 93 (1-2), 237–246. 10.1002/cite.202000201.
- Perea-Moreno, M.-A., Samerón-Manzano, E., Perea-Moreno, A.-J., 2019. Biomass as Renewable Energy: Worldwide Research Trends. *Sustainability* 11 (3), 863. 10.3390/su11030863.
- Ramírez-Gómez, Á., 2016. Research needs on biomass characterization to prevent handling problems and hazards in industry. *Particulate Science and Technology* 34 (4), 432–441. 10.1080/02726351.2016.1138262.
- Snider, D.M., 2001. An Incompressible Three-Dimensional Multiphase Particle-in-Cell Model for Dense Particle Flows. *Journal of Computational Physics* 170 (2), 523–549. 10.1006/jcph.2001.6747.
- Solnordal, C.B., Kenche, V., Hadley, T.D., Feng, Y., Witt, P.J., Lim, K.-S., 2015. Simulation of an internally circulating fluidized bed using a multiphase particle-in-cell method. *Powder Technology* 274, 123–134. 10.1016/j.powtec.2014.12.045.
- Sung, W.C., Kim, J.Y., Chung, S.W., Lee, D.H., 2021. Effect of particle size distribution on hydrodynamics of pneumatic conveying system based on CPFD simulation. *Advanced Powder Technology* 32 (7), 2336–2344. 10.1016/j.apt.2021.05.010.
- Tannous, K., Lam, P.S., Sokhansanj, S., Grace, J.R., 2013. Physical properties for flow characterization of ground biomass from Douglas fir wood. *Part. Sci. Technol.* 31, 291–300.
- Tu, Q., Wang, H., 2018. CPFD study of a full-loop three-dimensional pilot-scale circulating fluidized bed based on EMMS drag model. *Powder Technology* 323, 534–547. 10.1016/j.powtec.2017.09.045.
- Turton, R., Levenspiel, O., 1986. A short note on the drag correlation for spheres. *Powder Technology* 47 (1), 83–86. 10.1016/0032-5910(86)80012-2.
- Woodruff, R.B., Kreider, P., Weimer, A.W., 2012. A novel brush feeder for the pneumatic delivery of dispersed small particles at steady feed rates. *Powder Technology* 229, 45–50. 10.1016/j.powtec.2012.06.002.
- Yang, N., Wang, W., Ge, W., Wang, L., Li, J., 2004. Simulation of Heterogeneous Structure in a Circulating Fluidized-Bed Riser by Combining the Two-Fluid Model with the EMMS Approach. *Ind. Eng. Chem. Res.* 43 (18), 5548–5561. 10.1021/ie049773c.

**Lucas Massaro Sousa** : Conceptualization, Methodology, Software Validation, Formal analysis, Investigation, Writing - Original Draft, Visualization. **Benjamin Amblard** : Conceptualization, Formal analysis, Investigation, Writing - Review & Editing, Visualization, Project administration. **Sina Tebianian** : Conceptualization, Formal analysis, Investigation, Writing - Review & Editing, Visualization, Supervision, Project administration



## Highlights

- Pneumatic injection of biomass was simulated by CFD MP-PIC method.
- Good agreement observed among experimental data and MP-PIC simulation results.
- Gas-solid hydrodynamics in the injection line is visualized from the simulations.
- Feeder performance is maintained for injector diameter larger than 0.02m.
- A feeder operation map is developed as a function of dimensionless parameters.

## Conflict of Interest

The authors confirm that they have no known conflict of interests to disclose.